Ultrasonics Sonochemistry 93 (2023) 106301

Contents lists available at ScienceDirect

Ultrasonics Sonochemistry

journal homepage: www.elsevier.com/locate/ultson

Investigation on the cavitation bubble collapse and the movement characteristics near spherical particles based on Weiss theorem

Xiaoxiao Zheng [a], Xiaoyu Wang [a], Zhiling Ding [a,b,c], Angjun Li [a,b,c], Xuan Lu [a,b,c], Yuning Zhang [a,*], Yuning Zhang [b,c,*]

[a] Key Laboratory of Power Station Energy Transfer Conversion and System (Ministry of Education), School of Energy Power and Mechanical Engineering, North China Electric Power University, Beijing 102206, China
[b] College of Mechanical and Transportation Engineering, China University of Petroleum-Beijing, Beijing 102249, China
[c] Beijing Key Laboratory of Process Fluid Filtration and Separation, China University of Petroleum-Beijing, Beijing 102249, China

ARTICLE INFO

Keywords:
Particles-bubble interaction
Weiss theorem
Collapse morphology
Bubble movement
Kelvin impulse
High-speed photography

ABSTRACT

In this paper, the cavitation bubble dynamics near two spherical particles of the same size are investigated theoretically and experimentally. According to the Weiss theorem, the flow characteristics and the Kelvin impulse are obtained and supported by the sufficient experimental data. In terms of the initial bubble position, the bubble size and the distance between the two particles, the collapse morphology and the movement characteristics of the bubble are revealed in detail. The main findings include: (1) Based on a large number of experimental results, it is found that the Kelvin impulse theoretical model established in this paper can effectively predict the movement characteristics of the cavitation bubble near two particles of the same size. (2) When the initial bubble position is gradually away from the particles along the horizontal symmetry axis near two particles of the same size, the movement distance of the bubble centroid in the first period increases first and then decreases. (3) When the initial position of the bubble centroid is at the asymmetric position near the two particles, the movement direction of the bubble centroid is biased towards the particle closer to the bubble, but not towards the center of this particle.

1. Introduction

When hydraulic machinery operates in sediment laden flow, the material surface of flow passage components often suffers cavitation damage [1–6], and the existence of particle swarm in the liquid will make bubble dynamics more complex [7–12]. To be specific, the existence of the particle swarm not only provides additional nuclei to increase the probability of cavitation events [13,14], but also affects the severity of the bubble collapse by affecting the bubble morphology, the jet and the bubble movement [15,16]. However, most of the existing studies focus on the cavitation bubble dynamics under the effect of a single particle [15–17]. The bubble dynamic behavior near the particle swarm may be more complex than that near a single particle, such as the non-uniform morphology of the bubble collapse, the jet direction and the movement distance of the bubble centroid. In this paper, the cavitation bubble dynamics near two particles are investigated theoretically and experimentally.

According to the effects of the particle swarm on the cavitation phenomena, existing studies can be categorized into two aspects: bubble morphology [15,16] and jet characteristics [25–32]. For the bubble morphology, Zhang et al. [15] experimentally studied three typical cases of the bubble collapse morphology near a single spherical particle. And the parameter identification criteria for different cases is defined based on numerous experimental results. Recently, Wang et al. [16] theoretically investigated the cavitation bubble dynamics under the effect of a single particle in the bubble expansion and collapse process, and found that the particle could delay the expansion and collapse speed of the local bubble wall, which led to the non-uniformity of the bubble collapse.

For the jet characteristics, the Kelvin impulse has become a set of complete theories to predict the jet direction [16,28,29]. A brief review of the development of the Kelvin impulse will be given. Blake et al. [18–22] established a set of rigorous Kelvin impulse theory systems, and

* Corresponding authors at: Key Laboratory of Power Station Energy Transfer Conversion and System (Ministry of Education), School of Energy Power and Mechanical Engineering, North China Electric Power University, Beijing 102206, China (Y. Zhang). College of Mechanical and Transportation Engineering, China University of Petroleum-Beijing, Beijing 102249, China (Y. Zhang).
E-mail addresses: yuning.zhang@foxmail.com (Y. Zhang), zynlzyn.100@163.com (Y. Zhang).

https://doi.org/10.1016/j.ultsonch.2023.106301
Received 12 November 2022; Received in revised form 25 December 2022; Accepted 12 January 2023
Available online 13 January 2023

Nomenclature

Roman letters

$\boldsymbol{F}$	the action force on the bubble (kg·m/s^2)
g	the gravitational acceleration (m/s^2)
$\boldsymbol{I}$	the Kelvin impulse (kg·m/s)
L	the distance between the particle center and the initial position of the bubble centroid (m)
L_1	the distance between the center of the particle 1 and the initial position of the bubble centroid (m)
L_2	the distance between the center of the particle 2 and the initial position of the bubble centroid (m)
m	the strength of the bubble source (m^3/s)
R	the instantaneous bubble radius (m)
$\dot{R}$	the first derivative of R with respect to the time (m/s)
$\ddot{R}$	the second derivative of R with respect to the time (m/s^2)
R_0	the equilibrium bubble radius (m)
R_{max}	the maximum bubble radius (m)
R_{p1}	the radius of the particle 1 (m)
R_{p2}	the radius of the particle 2 (m)
r	the position of any point in the flow field (m)
r_0	the initial position of the bubble centroid
t	the time (s)
T	the first period of the bubble oscillation (s)
$\boldsymbol{u}$	the liquid velocity (m/s)
V	the volume of the bubble

Greek letters

κ	the polytropic exponent
ρ	the liquid density (kg/m^3)
σ	the surface tension coefficient (kg/s^2)
ϕ	the liquid velocity potential only caused by the bubble (m^2/s)
ϕ'	the additional liquid velocity potential caused by other wall surfaces except the cavitation bubble (m^2/s)
ψ	the liquid velocity potential (m^2/s)

regarded the bubble as a point source with variable source strength. And the effect of the wall can be reflected by the liquid velocity potential. On this basis, the possibility of predicting the bubble deformation according to the Kelvin impulse is proposed [23]. After that, Best and Blake [24,25] derived a simplified version expression of the Kelvin impulse based on the Lagally theorem. Furthermore, according to the Weiss theorem [26], the specific expression of the Kelvin impulse near a spherical particle is obtained. For more specific details of the above development process of the Kelvin impulse, readers can refer to the latest review [27]. Recently, Wang et al. [16] employed the Kelvin impulse to reveal the cavitation bubble characteristics near a single spherical particle with the experimental verification, and the application range of the Kelvin impulse according to the requirements of the quasi-spherical bubble is further given. In addition, many researchers have also made many contributions to the bubble movement characteristics or jet dynamics near a single particle through experiments and numerical simulation [30–34].

The previous studies mainly focus on the effect of a single particle on a cavitation bubble [15–17]. The bubble dynamic behavior near particle swarm may be more complex than that near a single particle, such as the morphology characteristics of the bubble collapse, the jet direction and the movement distance of the bubble centroid. In this paper, according to the Weiss theorem and sufficient experimental data, taking two particles as an example, the cavitation bubble dynamics near the particles are investigated theoretically and experimentally.

2. Theoretical model

In this section, according to the Weiss theorem and the Kelvin impulse [18–26], the theoretical model (including the basic equations, the solution method and the Kelvin impulse) will be introduced in detail. The main assumptions employed in this paper can be concluded as follows. The liquid is considered incompressible. The flow field is potential flow. In addition, the cavitation bubble is considered as a point source with the variable source strength and the fixed position. Moreover, the effects of the particles on the bubble are only reflected by the liquid velocity potential. And the effect between two particles is ignored. Furthermore, the bubble basically remains quasi-spherical during most of the bubble oscillation.

2.1. Basic equations and solutions

Based on the definition of the velocity potential, the liquid velocity $\boldsymbol{u}$ around the cavitation bubble and two particles can be demonstrated as follows [35]:

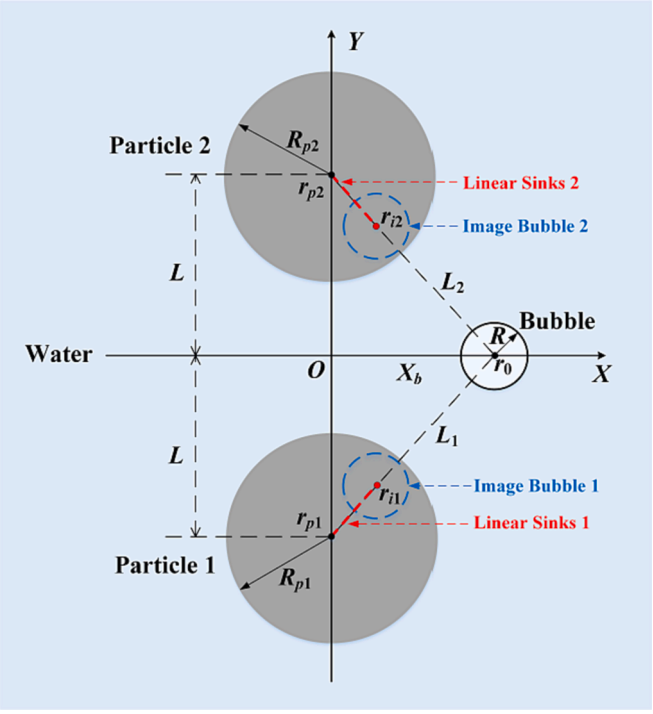

Fig. 1. A diagram of a system consisting of two spherical particles and a single cavitation bubble based on the Weiss theorem [24].

$$\boldsymbol{u} = \frac{\partial \psi}{\partial x}\boldsymbol{e}_x + \frac{\partial \psi}{\partial y}\boldsymbol{e}_y \tag{1}$$

where

$$\psi = \phi + \phi' \tag{2}$$

Here, ψ is the liquid velocity potential. ϕ is the liquid velocity potential produced by the bubble. ϕ' is the liquid velocity potential produced by the walls around the bubble. $\boldsymbol{e}_x$ and $\boldsymbol{e}_y$ are unit vectors pointing toward the positive direction of the X-axis and Y-axis defined in Fig. 1, respectively.

In an infinite flow field, ϕ can be written as follows [24]:

$$\phi = -\frac{m}{4\pi}\frac{1}{|r-r_0|} \tag{3}$$

where

$$m = 4\pi R^2 \dot{R} \tag{4}$$

here, m is the liquid volume released from the point source in unit time, and it also represents the bubble source strength. r is the position of any point in the flow field. r_0 is the initial position of the bubble centroid. R is the instantaneous bubble radius. $\dot{R}$ is the first derivative of R with respect to the time.

According to the Weiss theorem [16,24], the effect of one particle on the liquid velocity potential can be characterized by an image bubble and uniformly distributed linear sinks inside the particle. Therefore, the effect of the particle can be equivalently replaced by the superposition of the liquid velocity potential of the image bubble and the uniformly distributed linear sinks. The above Weiss theorem can satisfy the boundary condition of the liquid velocity on the particle surface.

Fig. 1 shows the diagram of a system consisting of two spherical particles, a single cavitation bubble and the surrounding liquid based on the Weiss theorem. A 2D coordinate system is established. The origin is the midpoint of the line between the centers of the two particles. And the Y-axis passes through the centers of the two particles. Two grey circles are the particles 1 and 2 with radii being R_{p1} and R_{p2}, respectively. The white circle is the cavitation bubble with a maximum radius of R_{max}. The blue area represents the water. In addition, L is the distance between the center of any particle and the origin. L_1 is the distance between the center of the particle 1 and the initial position of bubble centroid. L_2 is the distance between the center of the particle 2 and the initial position of bubble centroid. Two blue dashed circles represent the image bubbles 1 and 2, respectively. And two red dashed lines represent the uniform linear sinks 1 and 2, respectively. Moreover, the initial position of the bubble centroid r_0 is as follows:

$$r_0 = (x_0, \quad y_0) \tag{5}$$

The positions of the centers of particles 1 r_{p1} and 2 r_{p2} are as follows:

$$r_{p1} = (0, \quad -L) \tag{6}$$

$$r_{p2} = (0, \quad L) \tag{7}$$

r_{i1} and r_{i2} defined in Fig. 1 are the centroid positions of the image bubbles 1 and 2, respectively. The coordinates of r_{i1} and r_{i2} are as follows [24]:

$$r_{i1} = \left(\frac{R_{p1}^2 x_0}{L_1^2}, \quad \frac{R_{p1}^2(y_0+L)}{L_1^2} - L\right) \tag{8}$$

$$r_{i2} = \left(\frac{R_{p2}^2 x_0}{L_2^2}, \quad L - \frac{R_{p2}^2(L-y_0)}{L_2^2}\right) \tag{9}$$

Meanwhile, the position range of the uniform linear sinks 1 is from the center of the particle 1 to the centroid of the image bubble 1. The position range of the uniform linear sinks 2 is from the center of the particle 2 to the centroid of the image bubble 2 [24].

According to the above introduction, the liquid velocity potential induced by the two particles ϕ' can be obtained by the superposition of the velocity potential caused by particle 1 ϕ_1' and the velocity potential caused by particle 2 ϕ_1', thus ϕ' can be expressed as follows [24]:

$$\phi' = \phi_1' + \phi_2' \tag{10}$$

where

Table 1
Some important values of parameters employed for the numerical solution.

Physical parameters	Values	Units
p_0	1×10^5	Pa
κ	1.4	–
ρ	1×10^3	kg/m^3
σ	7.25×10^{-2}	kg/s^2

$$\phi_1' = -\frac{mR_{p1}}{4\pi L_1}\frac{1}{|r-r_{i1}|} + \frac{m}{4\pi R_{p1}}\int_0^{R_{p1}^2/L_1}\frac{ds}{\left|r-\left(\frac{s}{L_1}x_0, \frac{s}{L_1}(y_0+L)-L\right)\right|} \tag{11}$$

$$\phi_2' = -\frac{mR_{p2}}{4\pi L_2}\frac{1}{|r-r_{i2}|} + \frac{m}{4\pi R_{p2}}\int_0^{R_{p2}^2/L_2}\frac{ds}{\left|r-\left(\frac{s}{L_2}x_0, \frac{s}{L_2}(y_0+L)-L\right)\right|} \tag{12}$$

here, s represents the integral variable.

To close the above model, the classical Rayleigh—Plesset equation [16] is solved to calculate m in Eq. (4), and the equation is expressed as [16]:

$$R\ddot{R} + \frac{3}{2}\dot{R}^2 = \frac{1}{\rho}\left[\left(p_0 + \frac{2\sigma}{R_0}\right)\left(\frac{R_0}{R}\right)^{3\kappa} - \frac{2\sigma}{R} - p_0\right] \tag{13}$$

here, $\ddot{R}$ is the second derivative of R at t. p_0 is the ambient pressure. σ is the surface tension coefficient. R_0 is the equilibrium bubble radius. κ is the polytropic exponent. To obtain the values of R,$\dot{R}$, $\ddot{R}$ and the corresponding t, the fourth-fifth order Runge-Kutta method in MATLAB is employed to numerically solve Eq. (13). Some important values of parameters employed for the numerical solution are demonstrated in Table 1.

According to the above introduction, the effect of the bubble on the flow field is considered as a point source. Although the isotropic bubble wall motion equation Eq. (13) is selected to calculate the strength of the point source, it can also be employed to investigate the dynamic behavior of the quasi-spherical bubble with slight deformation. This is because the superposition of the liquid velocity potential induced by the image bubble and the uniform linear sinks will affect the distribution of the liquid equipotential surface around the bubble, which can also qualitatively reflect the morphological characteristics of the quasi-spherical bubble.

The calculation method of $\boldsymbol{u}$ can be concluded as follows. Firstly, the value of m can be obtained by simultaneous Eqs. (4) and (13). Secondly, ϕ and ϕ' can be calculated by simultaneous Eqs. (3) and (10)-(12). Finally, $\boldsymbol{u}$ can be obtained by taking the values of ϕ and ϕ' into Eqs. (1) and (2).

2.2. Kelvin impulse of the cavitation bubble

Blake et al. [18,22] systematically derived the Kelvin impulse $\boldsymbol{I}$ based on the Reynolds transmission theorem, and $\boldsymbol{I}$ can be defined as follows [18,22]:

$$\boldsymbol{I} = \oint_S \psi \boldsymbol{n} dS \tag{14}$$

here, $\boldsymbol{n}$ is the unit vector pointing inside the bubble. S is the bubble surface. $\boldsymbol{I}$ varies with the action force on the cavitation bubble $\boldsymbol{F}$, and $\boldsymbol{F}$ can be determined as follows [18]:

$$\boldsymbol{F} = d\boldsymbol{I}/dt \tag{15}$$

where

$$\boldsymbol{F} = \boldsymbol{F}_g + \boldsymbol{F}_b \tag{16}$$

$$\boldsymbol{F}_g = \rho g V \boldsymbol{e}_y \tag{17}$$

$$\boldsymbol{F}_b = \rho \int_S \left(\frac{1}{2} |\nabla \psi|^2 \boldsymbol{n} - (\boldsymbol{n} \cdot \nabla \psi) \nabla \psi \right) dS \tag{18}$$

here, $\boldsymbol{F}_g$ and $\boldsymbol{F}_b$ are the buoyancy and the Bjerknes force of the bubble, respectively. ρ is the liquid density. g is the gravitational acceleration. V is the bubble volume. ∇ is the Hamiltonian operator. According to the previous work of Blake et al. [19,22], when the volume of the bubble is small, the magnitude of the buoyancy is extremely small compared with the Bjerknes force. Thus the effect of the buoyancy on the Kelvin impulse is safely ignored in the following discussion [20,22].

According to the unsteady Lagally theorem of the deformable body [26], Best et al. [24] developed a simplified Bjerknes force $\boldsymbol{F}_b$ as follows [24]:

$$\boldsymbol{F}_b = -m\rho \nabla \phi'(r_0) \tag{19}$$

By simultaneous Eqs. (4), (9) and (14), the expression of the Kelvin impulse can be simplified as follows [16,24]:

$$\boldsymbol{I} = \pi \rho 4 \nabla g(r_0) \int_0^T R^4 \dot{R}^2 dt \tag{20}$$

where

$$g(r_0) = -\frac{4\pi}{m} \phi' \tag{21}$$

By simultaneous Eqs. (4), (10)-(12), (20) and (21), the values of the Kelvin impulse with different parameters can be easily derived.

2.3. Applicability range of theoretical model

According to the above introduction, the effect of the anisotropic perturbation of the liquid velocity potential caused by the particles on the bubble wall motion equation Eq. (13) is neglected. Hence, the theoretical model is applicable to the bubble close to the sphere. And the sphericity of the bubble is affected by both time and space. For example, when the bubble is very close to the particle, it may cause serious deformation of the bubble. In addition, the bubble may also be severely deformed at the end of the collapse because the jet injection may occur in this process. For the above situations, the theoretical model is not suitable for the calculation.

Based on our previous work [16], the applicability range of the theoretical model is quantitatively described with the aid of the high-speed photography experiment. In the pictures of the cavitation bubble obtained by the high-speed photography, the roundness of the cross-section of the bubble χ is calculated and employed to qualitatively characterize the sphericity of the bubble. And χ can be defined as follows [16]:

$$\chi = \frac{4\pi A}{P^2} \tag{22}$$

here, A is the area of the cross-section of the bubble. P is the perimeter of the cross-section of the bubble. The dimensionless distance between the bubble and the particle closer to the bubble γ is defined as follows [16]:

$$\gamma = \frac{\sqrt{(L - Y_b)^2 + X_b^2} - R_p}{R_{\max}} \tag{23}$$

here, Y_b is the vertical distance between the initial position of the bubble centroid and the origin of the coordinate system. R_p represents the radius of any one of two particles of the same size. According to our previous work [16], considering the effects of the time and the space on χ, when χ is greater than a critical value (e.g. 0.80), the bubble is considered to be quasi-spherical. Otherwise, the bubble is considered not to satisfy the condition of quasi-spherical. Based on a large number of experimental data, the critical value of γ is 0.5 [16]. And it can ensure that the bubble remains quasi-spherical for most of the time during the bubble growth and collapse. Hence, the following theoretical calculations are all guaranteed to satisfy the condition of $\gamma > 0.50$.

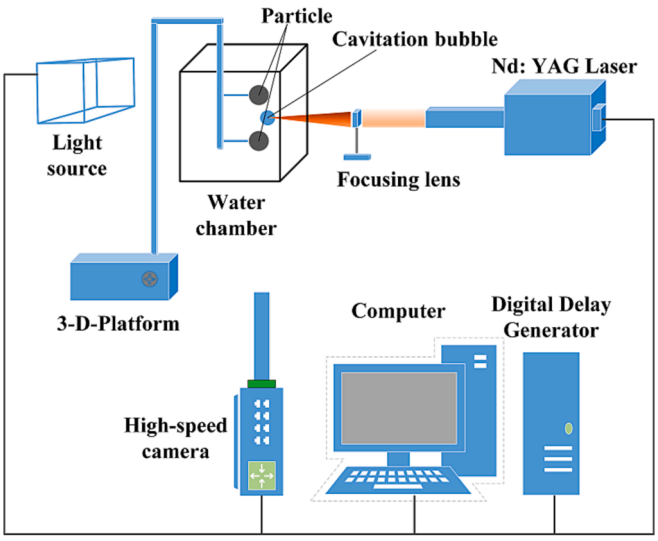

Fig. 2. A brief diagram of the experimental system in this paper.

Table 2
The specific information of main experimental equipment.

Names	Models	Manufacturers
Nd: YAG laser generator	Penny-100-S	Anshan Ziyu Laser Technology limited company
high-speed camera	Phantom v1212	Fuhuang Junda Gaoke Information Technology limited company
Focusing lens	LMH-10X-532	Etmont Optics (Shenzhen limited company)

3. Experimental setup and typical experimental examples

In this section, the experimental setup and a typical example of experimental results is demonstrated in detail.

3.1. High-speed photography

Fig. 2 shows a brief diagram of the experimental system. The specific information of the main experimental equipment is demonstrated in Table 2. And the experimental system can be divided into three parts, which are described as follows.

First, the module of cavitation bubble-particles interaction will be introduced as follows. Experiments are carried out in a water chamber filled with deionized water. When a high energy laser from Nd: YAG laser generator is focused through a focusing lens in the water chamber, a plasma is generated and gradually expands into a cavitation bubble. Two spherical particles of the same size are glued to the tips of two thin needles, and the two thin needles are attached to a three dimensional movement platform.

Then, the module of data acquisition will be described as follows. The complete process of cavitation bubble dynamics is captured by the high-speed camera. To prevent the laser light scattered by the liquid from damaging the lens of the camera, a filter is placed in front of the lens, which can filter 532 nm laser to protect the lens.

Finally, the modulation module of the experimental system will be introduced as follows. The relative position of the bubble and particles are controlled by a three dimensional movement platform, while the size of the bubble is adjusted by a laser energy attenuator in the laser beam

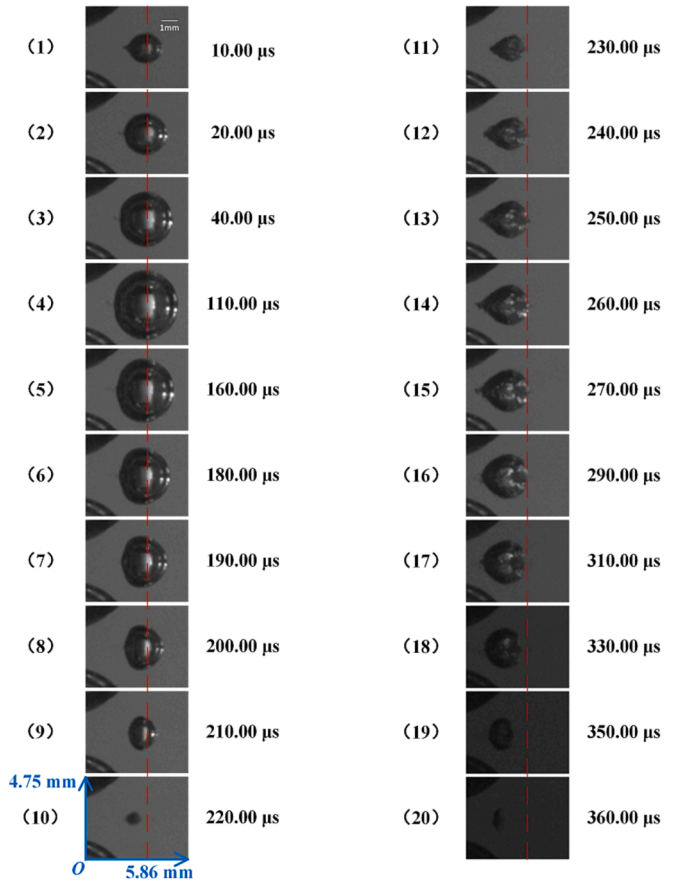

Fig. 3. A typical example of the cavitation bubble dynamics on the horizontal symmetrical axis of two spherical particles of the same size. The red dashed line refers to the initial position of the bubble centroid. The subfigure at the bottom left of the figure is marked with the actual length and the width of the subfigure. $X_b = 2.00$ mm, $Y_b = 0.00$ mm, $R_{max} = 1.73$ mm, $L = 2.63$ mm and $R_p = 2.00$ mm.

route. In addition, the laser generator, high-speed camera and flash are all synchronized by a digital delay generator to clearly record the complete process of the bubble-particles interaction.

3.2. Typical example of experimental results

Fig. 3 demonstrates a typical example of cavitation bubble dynamics on the horizontal symmetry axis near two particles of the same size. A pixel in the figure represents about 0.05×0.05 mm^2, and the parameter values related to experimental results are kept two significant digits after the decimal point. In the figure, twenty frames were selected to show the complete cavitation bubble dynamics in the first two bubble oscillation periods. And the sequence number and the corresponding time are marked on both sides of each subfigure. Moreover, the red dashed line in the figure refers to the initial position of the bubble centroid. As demonstrated in Fig. 3, in the expansion process of the first period (corresponding to subfigures 1–4), the bubble gradually expands until it reaches the maximum volume (corresponding to subfigure 4). The bubble almost remains spherical for the whole expansion process. Subsequently, the bubble gradually shrinks owing to the pressure difference inside and outside the bubble (corresponding to subfigures 5–9). According to the marked red dashed line, it is found that the bubble moves towards the middle position of the two particles, and the movement of the bubble centroid in the first period mainly occurs at the end of the collapse. The bubble wall shrinks unevenly under the effect of the two particles during the collapse (corresponding to subfigures 7–9), and the shrinkage velocity of the bubble wall near the particles is smaller than that of the bubble wall at other places. Moreover, a jet with the same direction as the bubble movement is generated by the bubble (corresponding to subfigures 14 and 15). After the first collapse, the bubble rebounds and collapses again (corresponding to subfigures 11–20) until the energy is completely dissipated.

Table 3
The comparison between the Kelvin impulse direction θ and the movement direction of the bubble centroid β with different initial positions of the bubble centroid.

Bubble positions		$\theta(^\circ)$	$\beta(^\circ)$	Δ
X_b(mm)	Y_b(mm)			
2.00	0.25	21.78	23.06	5.85 %
2.00	0.50	38.66	36.60	−5.32 %
2.00	1.00	45.00	41.33	−8.15 %
1.50	0.50	51.34	51.30	0.08 %

4. The cavitation bubble dynamics and the prediction of the Kelvin impulse.

In this section, the cavitation bubble dynamics at different positions near two particles of the same size are revealed. Based on the experimental results, the prediction of the Kelvin impulse on the direction of the jet or the bubble movement is verified.

According to the strict theoretical derivation by Best [28], it is found that the direction of the Kelvin impulse is consistent with the jet direction and the movement direction of the bubble centroid under certain conditions. Readers can refer to Eq. (3.6.3) in Reference 28 for more derivation details. Therefore, the movement direction of the bubble centroid is consistent with the jet direction. Tagawa et al. [29] and Wang et al. [16] replaced the jet direction with the movement direction of the bubble centroid in their own research. Due to the limitations of the experimental conditions, it is difficult to capture the experimental results of the jet appearance. Therefore, in the subsequent analysis, the prediction of the movement direction of the bubble centroid by the Kelvin impulse near two particles is mainly studied.

When the initial position of the bubble centroid is located on the horizontal symmetry axis near two particles of the same size, it is obvious that both the direction of the Kelvin impulse and the movement direction of the bubble centroid are toward the middle position of the two particles. When the initial position of the bubble centroid is on the vertical symmetry axis near the two particles, both the direction of the Kelvin impulse and the movement direction of the bubble centroid are toward the center of the particle closer to the bubble. Therefore, in the subsequent analysis of this section, the direction of the Kelvin impulse and the movement direction of the bubble centroid are investigated when the initial position of the bubble centroid is located at the asymmetric position near the two particles.

To quantitatively compare the direction of the Kelvin impulse and the movement direction of the bubble centroid, the angle between the movement direction of the bubble centroid and the negative horizontal direction is represented by β. The angle between the direction of the Kelvin impulse and the negative horizontal direction is represented by θ. Table 3 shows the comparison between θ and β with different initial position of the bubble centroid. The dimensionless difference between θ and β is defined as follows:

$$\Delta = \frac{\beta - \theta}{\theta} \tag{24}$$

In Table 3, in addition to the initial position of the bubble centroid (X_b and Y_b) given in the table, the first three rows in the table have the same parameter values with $R_{max} = 1.28$ mm, $L = 2.95$ mm and $R_p = 1.50$ mm. Other parameter values in the fourth row of the table are $R_{max} = 0.73$ mm, $L = 2.85$ mm and $R_p = 2.00$ mm. As demonstrated in Table 3, the dimensionless differences between θ and β for different initial

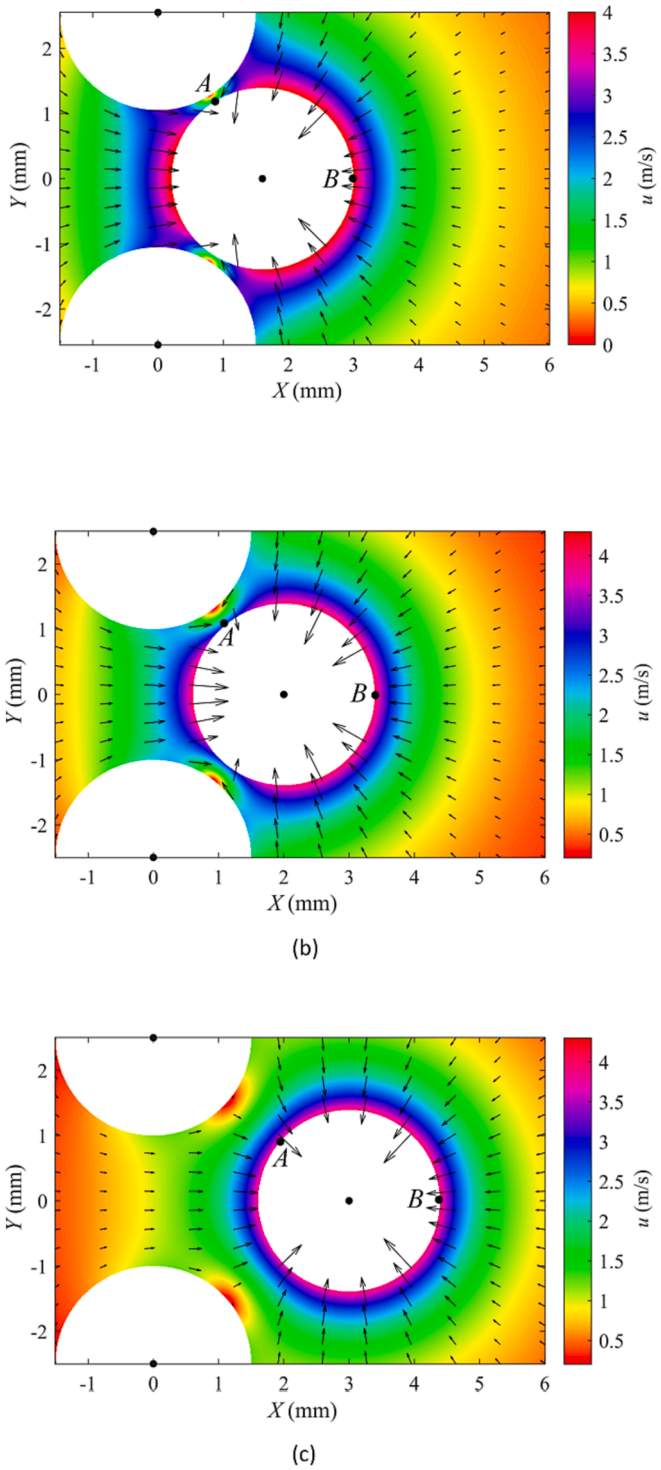

Fig. 4. The liquid velocity distribution around the bubble and two particles with different initial bubble positions. The colors in the figure represent the size of the liquid velocity. Point A represents the bubble wall closest to the particles. Point B represents the rightmost bubble wall. Subfigures (a), (b) and (c) refer to $X_b = 1.50$ mm, $X_b = 2.00$ mm and $X_b = 3.00$ mm, respectively. $R_{max} = 1.50$ mm. $L = 2.50$ mm.

position of the bubble centroid are small. Therefore, it can be concluded that the Kelvin impulse can effectively predict the jet direction and the movement direction of the bubble centroid. Furthermore, according to the values of θ and β, it can be found that the moving direction of the bubble centroid is toward the particle closer to the bubble, but not toward the center of this particle.

Table 4
The size of the liquid velocity at points A and B ($|\boldsymbol{u}_A|$ and $|\boldsymbol{u}_B|$) and their dimensionless difference with different X_b based on the theoretical results.

X_b(mm)	$\lvert\boldsymbol{u}_A\rvert$(m/s)	$\lvert\boldsymbol{u}_B\rvert$(m/s)	$\lvert\Delta\boldsymbol{u}^*\rvert$
1.50	1.67	4.07	58.97 %
2.00	2.84	4.03	29.53 %
3.00	3.78	3.97	4.79 %

5. Morphology characteristics of the cavitation bubble collapse

In this section, according to the enough experimental results and the liquid velocity obtained from Eq. (1), in terms of X_b, L and R_{max}, the quasi-spherical morphology characteristics of the bubble collapse on the horizontal symmetrical axis near two particles are revealed within the parameters satisfying the theoretical model [16]. In addition, the influences of the aforementioned parameters are fully discussed in the following two aspects. First, the liquid velocity distribution and the motions of bubble boundary and centroid are qualitatively displayed and compared. Second, the differences in the liquid velocities at several characteristic positions around the bubble wall and the shrinkage rates of the characteristic positions of the bubble wall are quantitatively shown, respectively. And the values of Y_b and R_p involved in this section are $Y_b = 0.00$ mm and $R_p = 1.50$ mm.

5.1. Influences of the initial bubble position

Fig. 4 demonstrates the liquid velocity $\boldsymbol{u}$ distribution around the cavitation bubble and particles with different initial bubble positions X_b. The colors in the figure represent the size of the liquid velocity. Point A represents the bubble wall closest to the particles. Point B represents the rightmost bubble wall. Subfigures (a), (b) and (c) refer to $X_b = 1.50$ mm, $X_b = 2.00$ mm and $X_b = 3.00$ mm, respectively. Other relevant important parameters are $R_{max} = 1.50$ mm and $L = 2.50$ mm. The white circle in the figure represents the bubble, and two white semicircles in the figure represent two particles of the same size. The length and the direction of the arrow represent the size and the direction of $\boldsymbol{u}$. In order to satisfy the quasi-spherical condition, the time corresponding to 70 % of the first oscillation period calculated by Eq. (13) was selected for the analysis, because based on the experimental results, it is found that the non-spherical characteristics of the bubble near this time were found initially. As demonstrated in Fig. 4, the difference in $|\boldsymbol{u}|$ around the bubble wall is obvious. Specifically, $|\boldsymbol{u}|$ at point A is obviously lower than that at point B. According to the continuity equation, the shrinkage rate of the bubble wall is consistent with the liquid velocity around the bubble wall if the mass transfer on the bubble surface is neglected. Hence, it can be inferred that the shrinkage rate of bubble wall near the point A is slightly smaller than that near the point B. Moreover, with the increase of X_b, the difference in $|\boldsymbol{u}|$ around the bubble wall is gradually weakened by comparing subfigures (a)-(c). In addition, the direction of $\boldsymbol{u}$ is toward the interior of the bubble during the bubble collapse, although the direction of the liquid velocity is not completely perpendicular to the bubble surface due to small errors.

To quantitatively show the difference of $|\boldsymbol{u}|$ around the bubble wall in Fig. 4, Table 4 demonstrates the size of the liquid velocity at points A and B (called $|\boldsymbol{u}_A|$ and $|\boldsymbol{u}_B|$ respectively) and their dimensionless difference with different X_b based on the theoretical results. The dimensionless difference between $|\boldsymbol{u}_A|$ and $|\boldsymbol{u}_B|$ is defined as follows:

$$|\Delta\boldsymbol{u}^*| = \frac{|\boldsymbol{u}_B| - |\boldsymbol{u}_A|}{|\boldsymbol{u}_B|} \tag{25}$$

As demonstrated in Table 4, with the increase of X_b, $|\boldsymbol{u}_A|$ increases gradually, while the change of $|\boldsymbol{u}_B|$ is weak due to the small influences of particles. And the value of $|\boldsymbol{u}_A|$ gradually approaches the value of $|\boldsymbol{u}_B|$, so $|\Delta\boldsymbol{u}^*|$ gradually decreases.

In addition, Fig. 5 demonstrates the motions of bubble boundary and

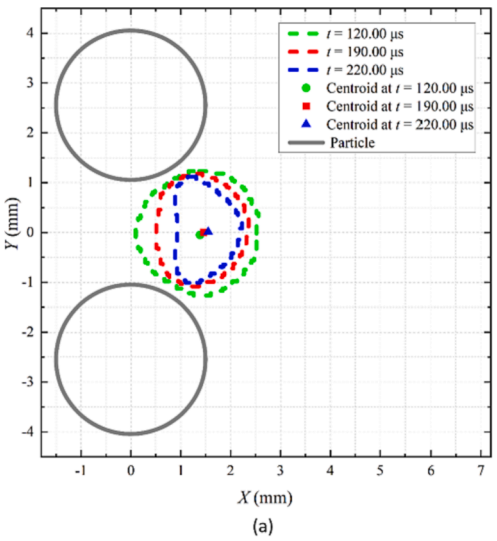

(a)

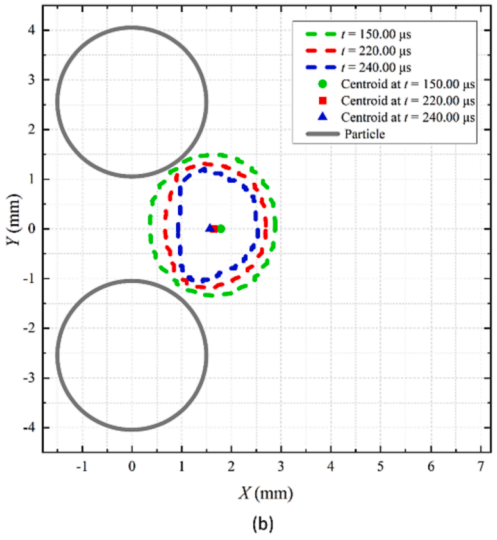

(b)

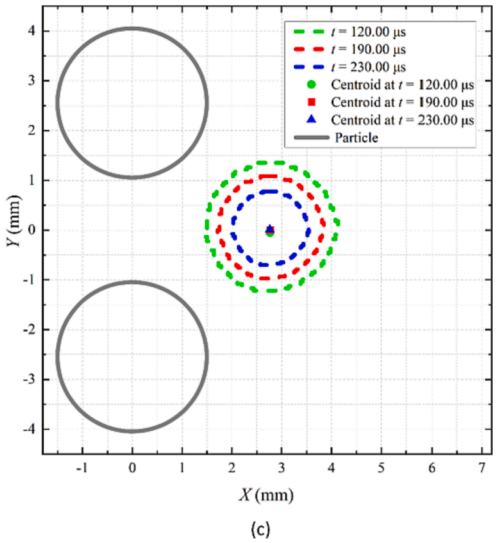

(c)

Fig. 5. The motions of bubble boundary and centroid at the first collapse stage with different X_b. Subfigures (a), (b) and (c) refer to $X_b = 1.50$ mm, $X_b = 2.00$ mm and $X_b = 3.00$ mm, respectively. $R_{max} = 1.50$ mm. $L = 2.50$ mm.

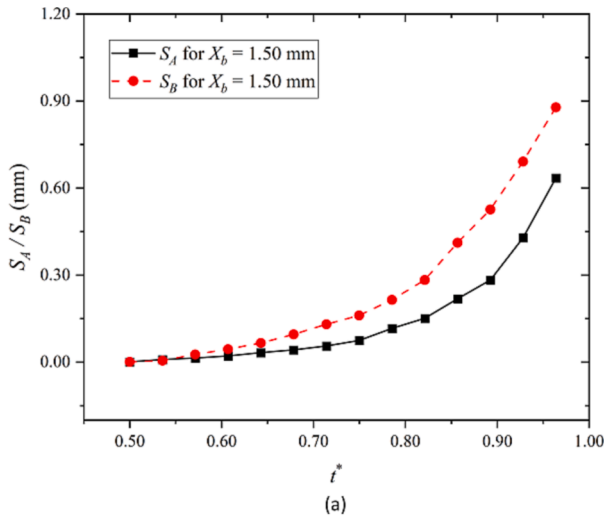

(a)

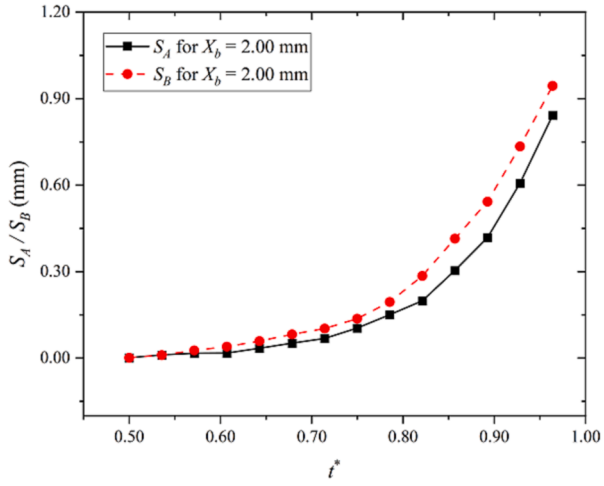

(b)

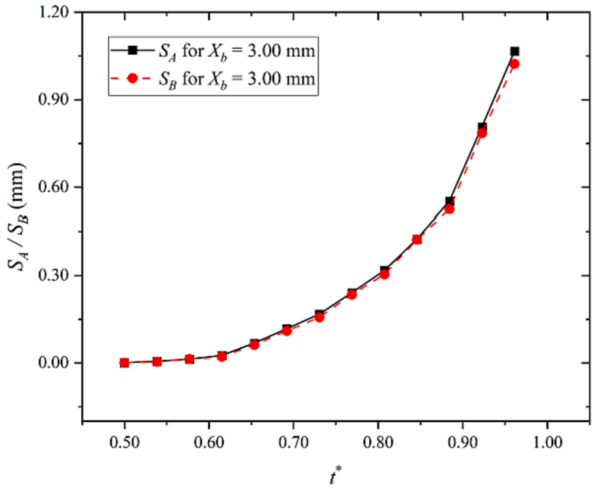

(c)

Fig. 6. The variations of the movement distances of the characteristic positions on the bubble wall (points A and B defined in Fig. 4) versus the dimensionless time of the bubble collapse t^* with different X_b. Subfigures (a), (b) and (c) refer to $X_b = 1.50$ mm, $X_b = 2.00$ mm and $X_b = 3.00$ mm, respectively. $R_{max} = 1.50$ mm. $L = 2.50$ mm.

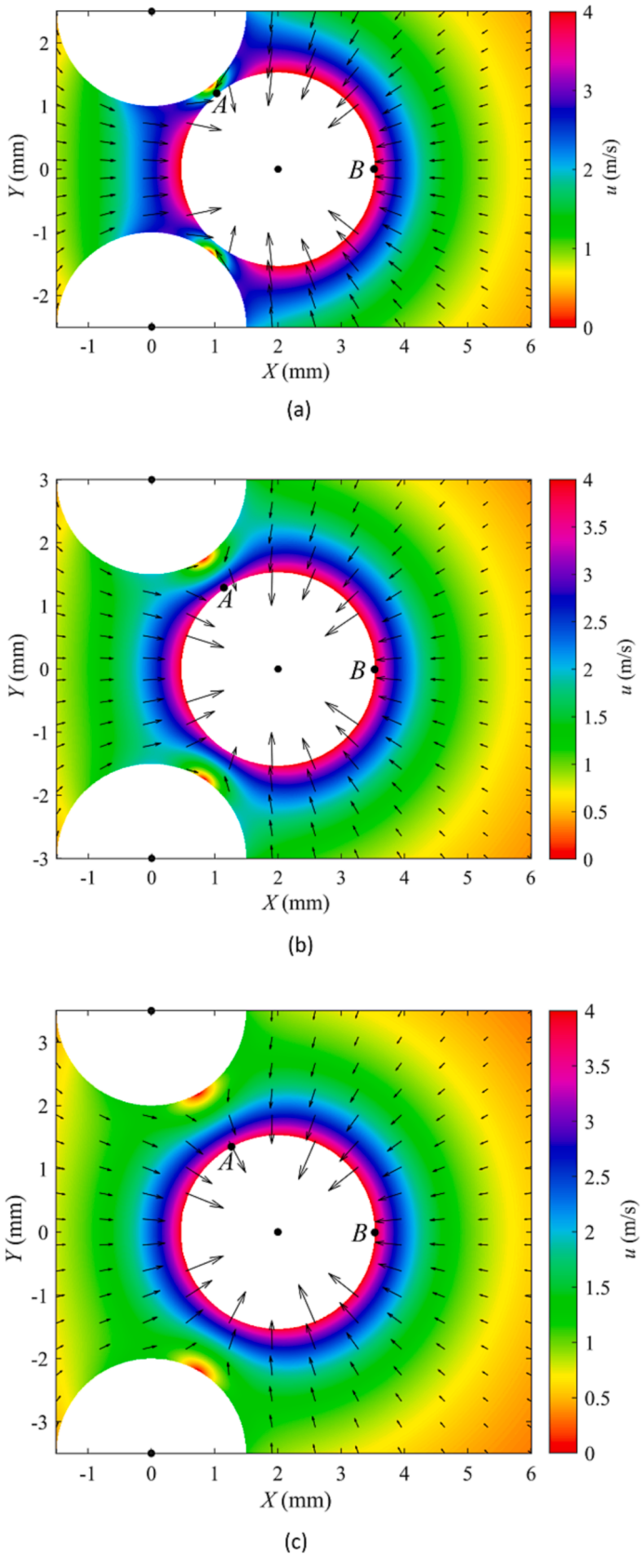

Fig. 7. The liquid velocity distribution around the bubble and two particles with different distance between two particles. The colors in the figure represent the size of the liquid velocity. Point *A* represents $\boldsymbol{u}$ around the bubble wall closest to the particle. Point *B* represents the liquid velocity around the rightmost bubble wall. Subfigures (a), (b) and (c) refer to $L = 2.50$ mm, $L = 3.00$ mm and $L = 3.50$ mm, respectively. $X_b = 2.00$ mm. $R_{max} = 1.68$ mm.

Table 5
The size of the liquid velocity at points A and B ($|\boldsymbol{u}_A|$ and $|\boldsymbol{u}_B|$) and their dimensionless difference with different L based on the theoretical results.

L(mm)	$\|\boldsymbol{u}_A\|$(m/s)	$\|\boldsymbol{u}_B\|$(m/s)	$\|\Delta\boldsymbol{u}^*\|$
2.50	2.03	4.05	49.88 %
3.00	3.42	4.01	14.66 %
3.50	3.74	3.99	6.15 %

centroid at three typical times with different X_b. Subfigures (a), (b) and (c) refer to $X_b = 1.50$ mm, $X_b = 2.00$ mm and $X_b = 3.00$ mm, respectively, which correspond to the cases in Fig. 4. And other relevant important parameters are $R_{max} = 1.50$ mm and $L = 2.50$ mm. The stability of the bubble size is ensured by precisely controlling the energy of incident laser As demonstrated in Fig. 5, the shrinkage rate of bubble wall near the particles is slightly smaller than that of other bubble walls. Moreover, with the increase of X_b, the bubble gradually tends to spherical shrinkage because the effects of the two particles gradually decreases. By comparing the results of Figs. 4 and 5, the basic trend of the morphological changes obtained from the experimental results is consistent with the prediction of $\boldsymbol{u}$ around the bubble wall.

In addition, based on the results in Fig. 5, Fig. 6 demonstrates the variations of the movement distances of the characteristic positions on the bubble wall (points A and B defined in Fig. 4) versus the dimensionless time t^* of the bubble collapse with different X_b. S_A and S_B represent the movement distances of the points A and B. And the definition of the dimensionless time t^* is as follows:

$$t^* = \frac{t}{T} \tag{26}$$

here, T is the first oscillation period of the bubble which can be numerically calculated by Eq. (13).

In Fig. 6, subfigures (a), (b) and (c) refer to $X_b = 1.50$ mm, $X_b = 2.00$ mm and $X_b = 3.00$ mm, respectively. And other relevant important parameters are $R_{max} = 1.50$ mm and $L = 2.50$ mm. As demonstrated in Fig. 6, when X_b is small, S_A is weaker than S_B at the early stage of the bubble collapse. With the increase of X_b, the difference between S_A and S_B gradually becomes smaller by comparing subfigures (a), (b) and (c). And this indicates that the bubble almost collapses in a spherical morphology.

5.2. Influences of the distance between two particles

Fig. 7 demonstrates the liquid velocity $\boldsymbol{u}$ distribution around the bubble and two particles with different distance between the two particles L. Subfigures (a), (b) and (c) refer to $L = 2.50$ mm, $L = 3.00$ mm and$L = 3.50$ mm, respectively. Other relevant important parameters are $X_b = 2.00$ mm and $R_{max} = 1.68$ mm. The time corresponding to 70 % of the first oscillation period calculated by Eq. (13) was selected for the analysis. As demonstrated in Fig. 7(a)-(c), with the increase of L, the difference in $|\boldsymbol{u}|$ around the bubble wall is gradually weakened, this indicates that the bubble gradually tends to spherical shrinkage because the influences of the two particles gradually decrease.

Moreover, based on the theoretical results in Fig. 7, Table 5 demonstrates the size of the liquid velocity at points A and B ($|\boldsymbol{u}_A|$ and $|\boldsymbol{u}_B|$) and their dimensionless difference with different L based on the theoretical results. As demonstrated in Table 5, with the increase of L, the influences of particles on the bubble is gradually weakened, $|\boldsymbol{u}_A|$ increases gradually, while $|\boldsymbol{u}_B|$ changes weakly, thus $|\Delta\boldsymbol{u}^*|$ gradually decreases, because $|\boldsymbol{u}_A|$ and $|\boldsymbol{u}_B|$ tend to be equal.

In addition, Fig. 8 demonstrates motions of bubble boundary and centroid at the first collapse stage with different L. Subfigures (a), (b) and (c) refer to $L = 2.50$ mm, $L = 3.00$ mm and $L = 3.50$ mm, respectively, which correspond to the cases in Fig. 7. And other relevant important parameters are $X_b = 2.00$ mm and $R_{max} = 1.68$ mm. As demonstrated in Fig. 8, with the increase of L, the influences of the

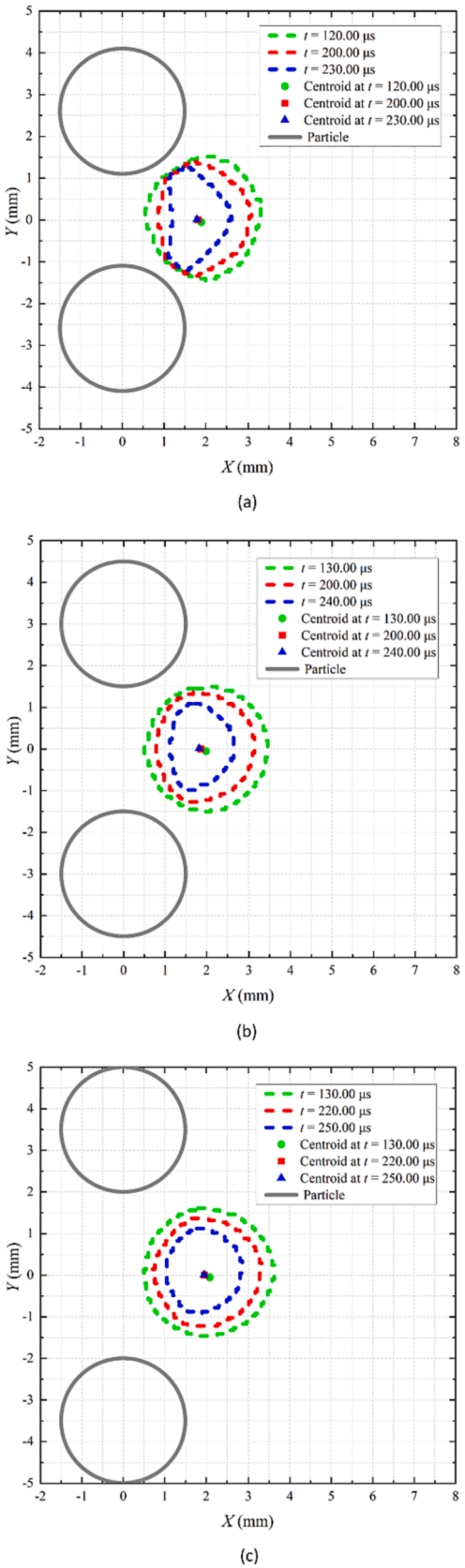

Fig. 8. The motions of bubble boundary and centroid at the first collapse stage with different L. Subfigures (a), (b) and (c) refer to $L = 2.50$ mm, $L = 3.00$ mm and $L = 3.50$ mm, respectively. $X_b = 2.00$ mm. $R_{max} = 1.68$ mm.

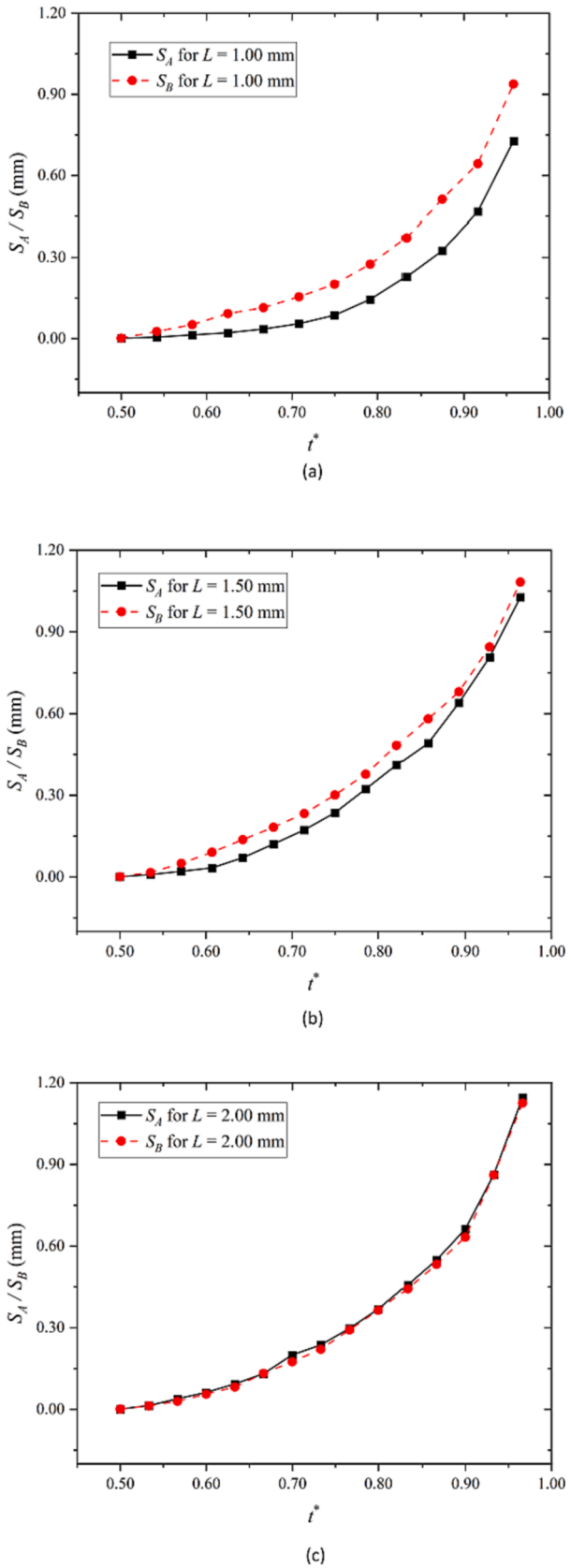

Fig. 9. The variations of the movement distances of the characteristic positions on the bubble wall (points A and B defined in Fig. 7) versus t^* with different L. Subfigures (a), (b) and (c) refer to $L = 2.50$ mm, $L = 3.00$ mm and$L = 3.50$ mm, respectively. $X_b = 2.00$ mm.$R_{max} = 1.68$ mm.

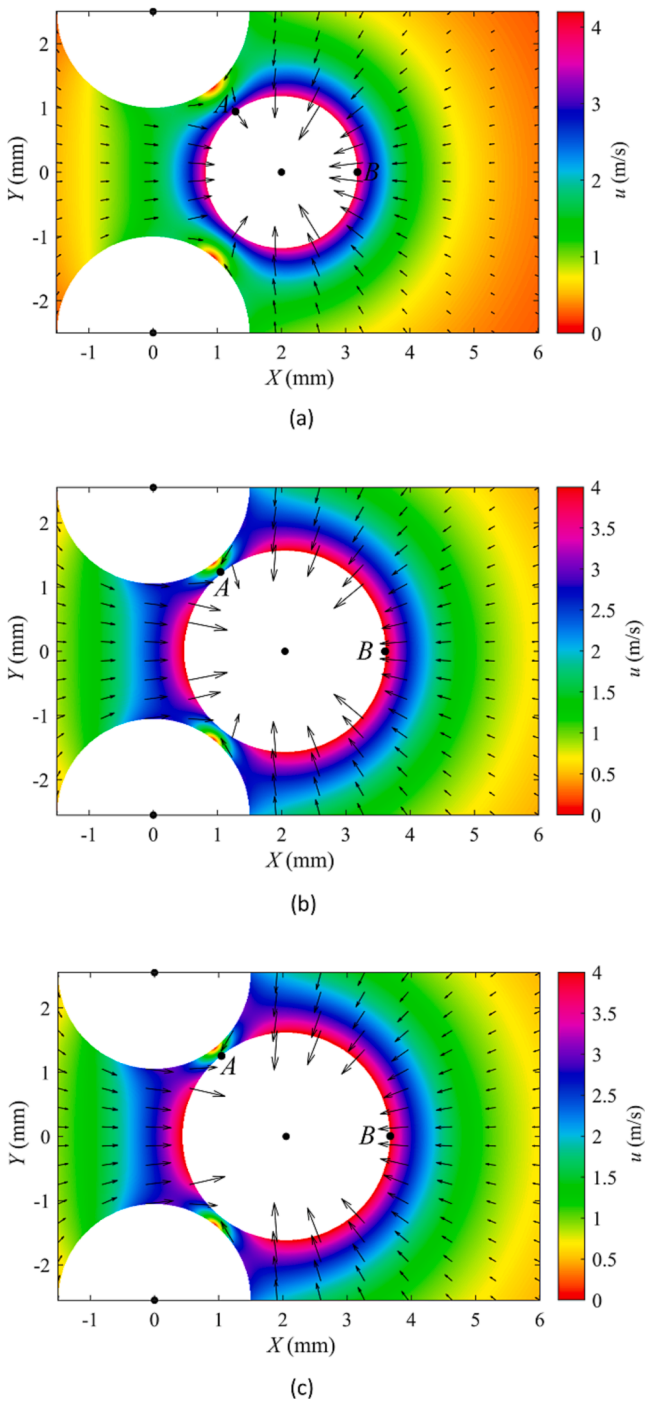

Fig. 10. The liquid velocity distribution around the bubble and two particles with different maximum radii of the bubbles. The colors in the figure represent the size of the liquid velocity. Point A represents the liquid velocity near the bubble wall closest to the particle. Point B represents the liquid velocity near the rightmost bubble wall. Subfigures (a), (b) and (c) refer to $R_{max} = 1.28$ mm, $R_{max} = 1.73$ mm and $R_{max} = 1.80$ mm, respectively. $X_b = 1.50$ mm. $L = 2.50$ mm.

particles on the bubble are weakened gradually. For example, the bubble appears spherical collapse with a large L as demonstrated in Fig. 8(c). Therefore, this supports the results predicted in Fig. 7.

Based on the experimental results in Fig. 8, Fig. 9 demonstrates the variations of the movement distances of the characteristic positions on the bubble wall (points A and B defined in Fig. 7) versus t^* with different L. S_A and S_B represent the movement distances of the points A and B.

Table 6
The size of the liquid velocity at points A and B ($|\boldsymbol{u}_A|$ and $|\boldsymbol{u}_B|$) and their dimensionless difference with different R_{max} based on the theoretical results.

R_{max}(mm)	$\|\boldsymbol{u}_A\|$(m/s)	$\|\boldsymbol{u}_B\|$(m/s)	$\|\Delta\boldsymbol{u}^*\|$
1.28	3.46	3.96	12.51 %
1.73	2.24	4.03	44.28 %
1.80	1.88	4.02	53.23 %

Subfigures (a), (b) and (c) refer to $L = 2.50$ mm, $L = 3.00$ mm and $L = 3.50$ mm, respectively. Other relevant important parameters are$X_b = 1.50$ mm and$R_{max} = 1.68$ mm. As demonstrated in Fig. 9, when the distance between two particles is small, the movement distance of the point A is not obvious at the early stage of the bubble collapse, while the movement distance of the point B is significant. In addition, with the increase of L, the differences between S_A and S_B gradually decrease at the early stage of the collapse by comparing subfigures (a), (b) and (c).

5.3. Influences of the bubble size

Fig. 10 demonstrates the liquid velocity $\boldsymbol{u}$ distribution around the bubble and two particles with different maximum radii of the cavitation bubbles R_{max}. Subfigures (a), (b) and (c) refer to $R_{max} = 1.28$ mm, $R_{max} = 1.73$ mm and $R_{max} = 1.80$ mm, respectively. Other relevant important parameters are $X_b = 1.50$ mm and $L = 2.50$ mm. The selection method of the time in this figure is the same as those in Figs. 4 and 7. As demonstrated in Fig. 10(a)-(c), as R_{max} gradually increases, the difference in $|\boldsymbol{u}|$ around the bubble wall is gradually significant due to the strong influences of the particles.

In addition, based on the theoretical results in Fig. 10, Table 6 demonstrates the size of the liquid velocity at points A and B ($|\boldsymbol{u}_A|$ and $|\boldsymbol{u}_B|$) and their dimensionless difference with different R_{max} based on the theoretical results. As demonstrated in Table 6, when R_{max} is small, the difference between $|\boldsymbol{u}_A|$ and $|\boldsymbol{u}_B|$ is not obvious due to the weak influences of the two particles. However, with the increase of R_{max}, the difference between $|\boldsymbol{u}_A|$ and $|\boldsymbol{u}_B|$ is gradually significant.

Fig. 11 demonstrates the motions of bubble boundary and centroid at the first collapse stage with different R_{max}. Subfigures (a), (b) and (c) refer to $R_{max} = 1.28$ mm, $R_{max} = 1.73$ mm and $R_{max} = 1.80$ mm, respectively, which correspond to the cases in Fig. 10. S_A and S_B represent the movement distances of the points A and B. And other relevant important parameters are $X_b = 1.50$ mm and $L = 2.50$ mm. As demonstrated in Fig. 11, due to the influence of the particles, there is a weak non-uniformity in the shrinkage rates of bubble wall during the bubble collapse. Moreover, with the increase of R_{max}, the non-uniformity of the shrinkage rate of the bubble wall is gradually significant, so this is also consistent with the liquid velocity distribution around the bubble and particles predicted by Eq. (1).

Based on the experimental results in Fig. 11, Fig. 12 demonstrates the variations of the movement distances of the characteristic positions on the bubble wall (points A and B defined in Fig. 10) versus t^* with different R_{max}. Subfigures (a), (b) and (c) refer to $R_{max} = 1.28$ mm, $R_{max} = 1.73$ mm and $R_{max} = 1.80$ mm, respectively. Other relevant important parameters are $X_b = 1.50$ mm and $L = 2.50$ mm. As demonstrated in Fig. 12, with the increase of R_{max}, the difference between S_A and S_B is gradually significant at the early stage of the bubble collapse by comparing subfigures (a), (b) and (c).

According to the above analysis, when the bubble collapses near two particles, the shrinkage rates of the bubble wall are uneven. The shrinkage rates of the bubble wall near the particles are smaller than those far away from the particles. Moreover, through qualitatively comparing the liquid flow characteristics predicted by Eq. (1) and the movement characteristics of the bubble wall obtained from experimental results with various parameters (the initial bubble position, the bubble size and the distance between two particles), it is found that the liquid velocity distribution predicted by Eq. (1) has a good predictive

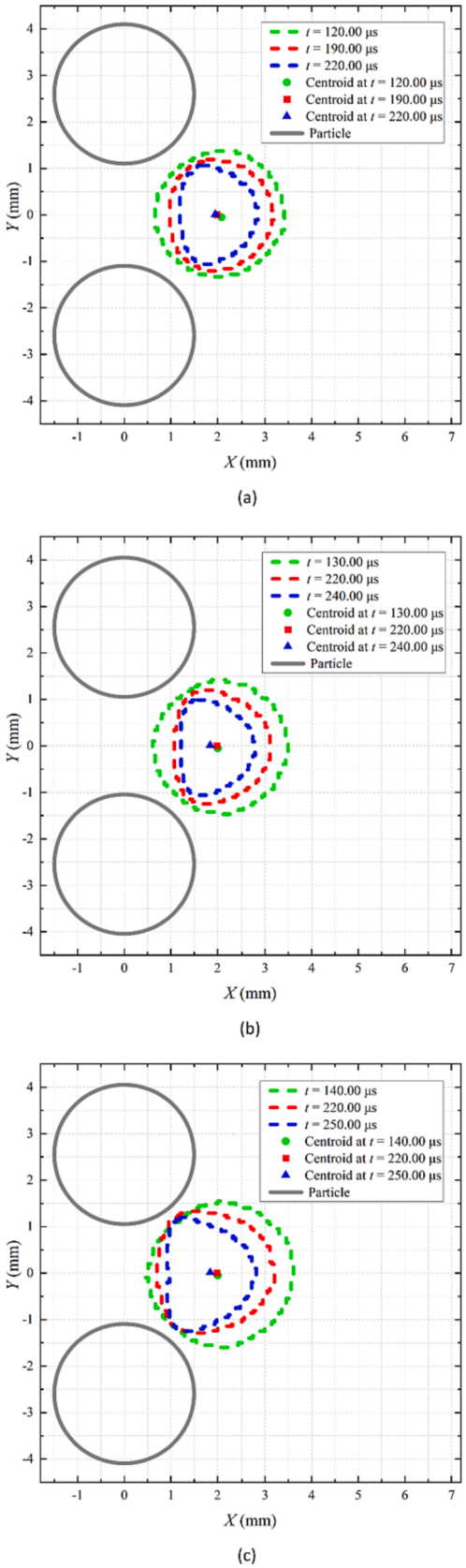

Fig. 11. The motions of bubble boundary and centroid at the first collapse stage with R_{max}. Subfigures (a), (b) and (c) refer to $R_{max} = 1.28$ mm, $R_{max} = 1.73$ mm and $R_{max} = 1.80$ mm, respectively. $X_b = 1.50$ mm. $L = 2.50$ mm.

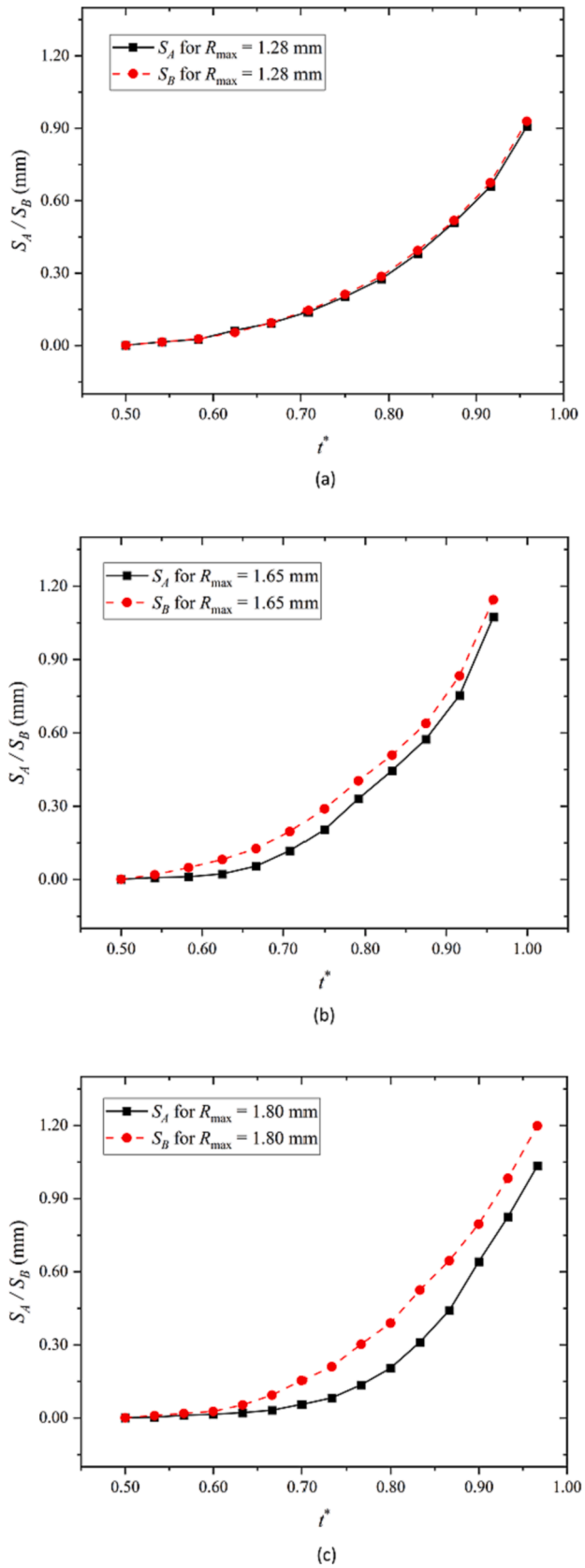

Fig. 12. The variations of the movement distances of the characteristic positions on the bubble wall (points A and B defined in Fig. 10) versus t^* with differentR_{max}. Subfigures (a), (b) and (c) refer to R_{max} = 1.28 mm, R_{max} = 1.73 mm and R_{max} = 1.80 mm, respectively. X_b = 1.50 mm. L = 2.50 mm.

value for the non-uniformity characteristics of the bubble collapse.

6. Movement characteristics of the cavitation bubble

In the present section, based on the Kelvin impulse obtained from Eqs. (20) and (21) and the movement distance of the bubble centroid d, in terms of X_b, L and R_{max}, the movement characteristics of the bubble on the horizontal symmetrical axis near two particles will be quantitatively investigated within the parameters satisfying the theoretical model [16]. Since the direction of the Kelvin impulse always points to the middle position of two particles of the same size, the size of the Kelvin impulse $|\boldsymbol{I}|$ is only analyzed in this section. The values of Y_b and R_p involved in this section are Y_b = 0.00 mm and R_p = 1.50 mm.

6.1. Influences of the distance between two particles

Fig. 13 demonstrates the variations of the absolute value of the Kelvin impulse $|\boldsymbol{I}|$ versus different initial bubble positions X_b with different distance between two particles L. The blue, red and black lines in the figure refer to L = 3.00 mm, L= 2.50 mm and L = 2.20 mm, respectively. R_{max} = 1.28 mm. As demonstrated in Fig. 13, when X_b is very small, the force exerted by the two particles on the cavitation bubble is offset, so $|\boldsymbol{I}|$ is almost zero. With the increase of X_b, $|\boldsymbol{I}|$ increases first and then decreases gradually. This is because when X_b is very far, $|\boldsymbol{I}|$ will become very small due to the weak influences of the particles on the bubble. In addition, the greater L, the smaller $|\boldsymbol{I}|$ due to the weak influences of the particles on the bubble.

Fig. 14 demonstrates the variations of the movement distance of the bubble centroid d versus X_b with the different L. The blue, red and black lines in the figure refer to L = 3.00 mm, L= 2.50 mm and$L$ = 2.20 mm, respectively. R_{max} = 1.28 mm. As demonstrated in Fig. 14, with the increase of X_b, d has a peak value. When X_b is very small or very large, d is very small due to the weak influences of the particles on the bubble. Moreover, d decreases with the increase of L. Furthermore, by comparing Figs. 13 and 14, it is found that the consistency of the basic trend of $|\boldsymbol{I}|$ and d versus X_b with the different L is great.

6.2. Influences of the bubble size

Fig. 15 demonstrates the variations of the absolute value of the Kelvin impulse $|\boldsymbol{I}|$ versus X_b with the different R_{max}. The blue, black and red solid lines in the figure refer to R_{max} = 1.80 mm, R_{max}= 1.28 mm and R_{max} = 1.65 mm, respectively. L = 2.50 mm. As demonstrated in Fig. 15, with the increase of X_b, $|\boldsymbol{I}|$ increases first and then decreases gradually. The reasons for the variations have been explained before, and will not be repeated here. Moreover, the greater R_{max}, the greater $|\boldsymbol{I}|$ due to the strong influences of the particles on the bubble.

Fig. 16 demonstrates the variations of the movement distance of the bubble centroid d versus X_b with the different R_{max}. The blue, black and red solid lines in the figure refer to R_{max} = 1.80 mm, R_{max}= 1.28 mm andR_{max} = 1.65 mm, respectively.L = 2.50 mm. As demonstrated in Fig. 16, with the increase of X_b, d increases gradually at first, and then decreases gradually after reaching a peak value. Moreover, the greater R_{max}, the greater d. By comparing Figs. 15 and 16, there is also good consistency of the general trend for the Kelvin impulse and bubble centroid movement versus X_b with the different R_{max}. Therefore, it can be concluded that the Kelvin impulse has a good qualitative predictive value for the movement trend of the bubble centroid.

7. Special cases

In the present section, To fully demonstrate the cavitation bubble dynamics on the symmetrical axis of two spherical particles of the same size, Figs. 17 and 18 show two special examples that do not satisfy the theoretical model [16]. As demonstrated in Fig. 17, the blue dashed line

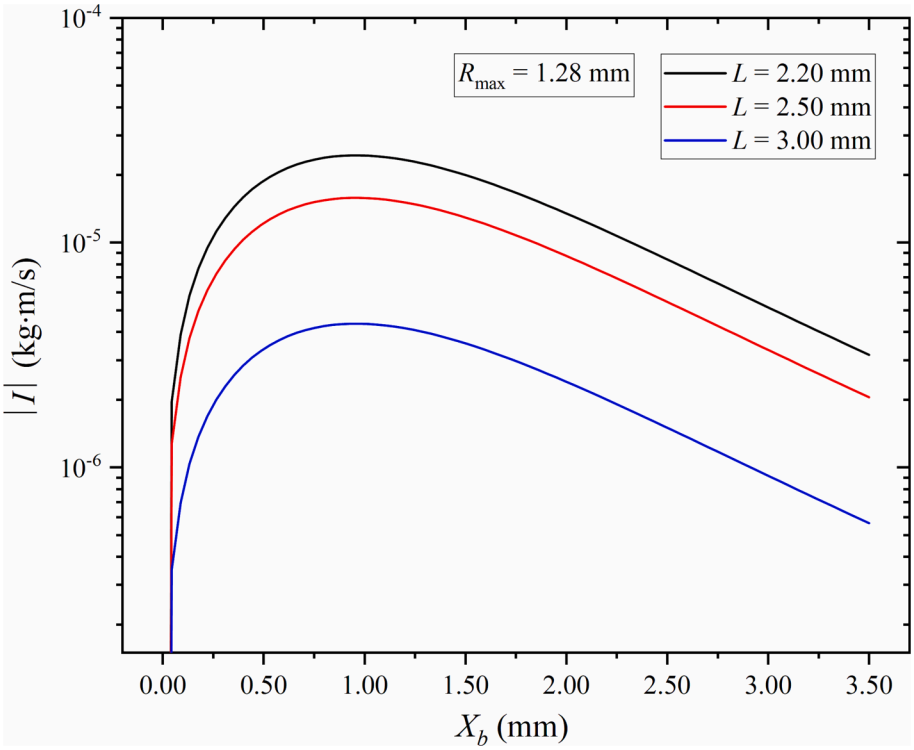

Fig. 13. The variations of the absolute value of the Kelvin impulse versus X_b with different L. The blue, red and black lines in the figure refer to L = 3.00 mm, L = 2.50 mm and L = 2.20 mm, respectively. R_{max} = 1.28 mm.

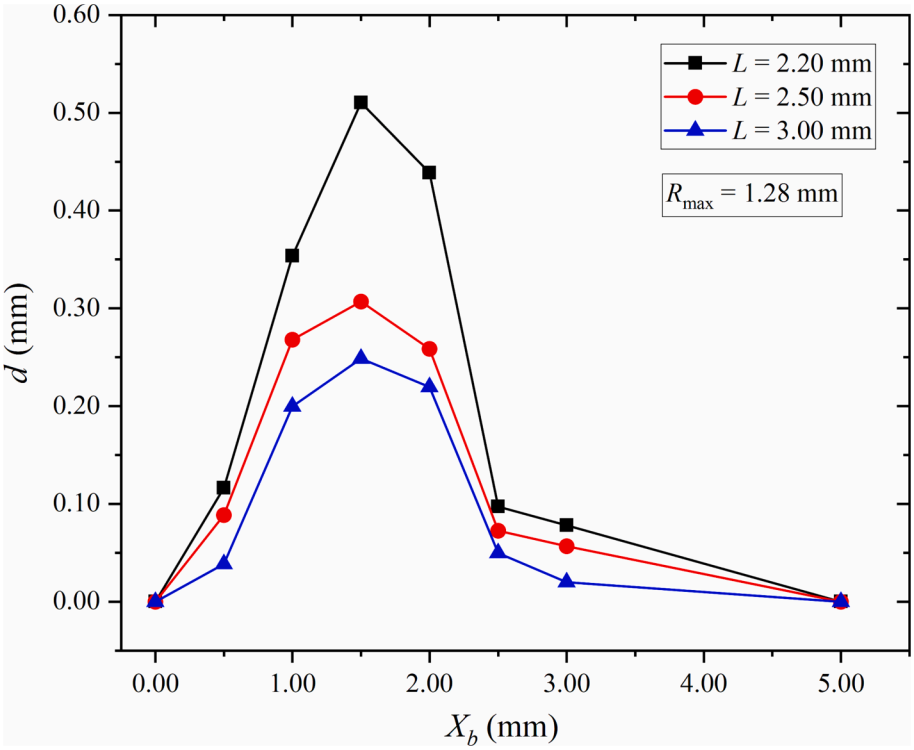

Fig. 14. The variations of the movement distance of the bubble centroid versus X_b with different L. The blue, red and black lines in the figure refer to L = 3.00 mm, L = 2.50 mm and L = 2.20 mm, respectively. R_{max} = 1.28 mm.

in the figure refers to the initial position of bubble centroid. X_b = 0.00 mm, Y_b = 0.00 mm, R_{max} = 1.80 mm, L = 2.00 mm and R_p = 1.50 mm. Since the initial bubble position is located in the middle position of two spherical particles of the same size, the left and right halves of the bubble are also symmetrical in the whole bubble oscillation process. Moreover, the shrinkage rate of bubble wall near the particles is obviously smaller than that of other bubble walls, so a "neck" is formed between two particles. In addition, since the effects of the two particles

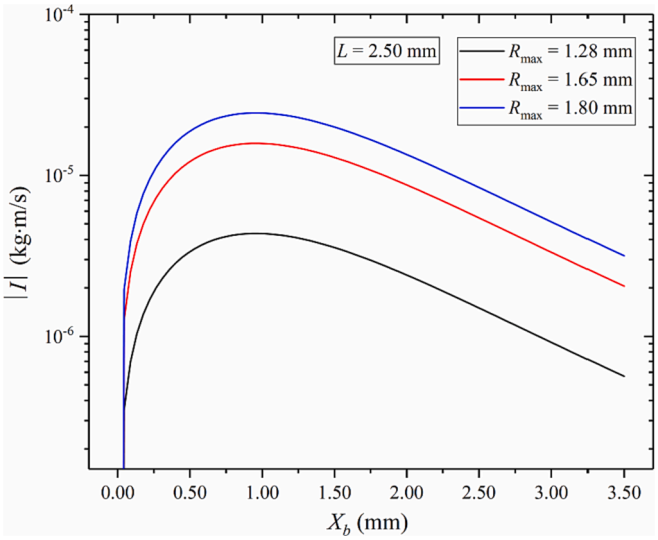

Fig. 15. The variations of the absolute value of Kelvin impulse versus X_b with different R_{max}. The blue, black and red solid lines in the figure refer to R_{max} = 1.80 mm, R_{max}= 1.28 mm and R_{max} = 1.65 mm, respectively. L = 2.50 mm.

on the cavitation bubble is offset, the bubble did not move. For the last part of the first bubble collapse, the bubble is split into two parts from its middle position (corresponding to subfigure 11). Subsequently, the two parts will rebound and collapse respectively until the bubble completely disappears.

Fig. 18 demonstrates the cavitation bubble dynamics on the symmetrical axis of two spherical particles of the same size with X_b = 1.00 mm, Y_b = 0.00 mm, R_{max} = 1.80 mm, L = 2.00 mm and R_p = 1.50 mm. It is worth noting that the morphology difference between the left and right halves of bubble is very significant in the whole process of bubble oscillations, and a curved "bridge" is formed between the two particles during the bubble collapse (corresponding to subfigures 10 and 15).

8. Conclusion

In this paper, the cavitation bubble dynamics near two spherical particles of the same size are theoretically investigated with the support of sufficient experimental data. The flow characteristics and the Kelvin impulse are obtained based on the Weiss theorem. In terms of the initial bubble position, the bubble size and the distance between two particles, the collapse morphology and the movement characteristics of the bubble are revealed in detail. In addition, several special cases of cavitation bubble dynamics that do not satisfy the theoretical model are also demonstrated. The major findings of this paper are concluded as follows:

(1). Based on a large number of experimental results, it is found that the results of the Kelvin impulse theoretical model established in this paper are in good agreement with the experimental results, which indicates that the theoretical model can effectively predict the movement characteristics of the cavitation bubble near two particles of the same size.

(2). When the initial bubble position is gradually away from the two vertically placed particles along the horizontal symmetry axis, the movement distance of the bubble centroid in the first period increases first and then decreases. The bubble will not move until the initial bubble position is far enough from the particles. The larger the distance between two particles is, the smaller the movement distance of the bubble centroid is. The larger the bubble size is, the greater the movement distance of the bubble centroid is.

(3). The liquid velocity at the gap between the bubble and the particles is lower than that at other places, which indicates that the shrinkage velocity of the bubble wall near the particles is lower than that at other places during the bubble collapse. The initial position of the bubble centroid, the bubble size and the distance

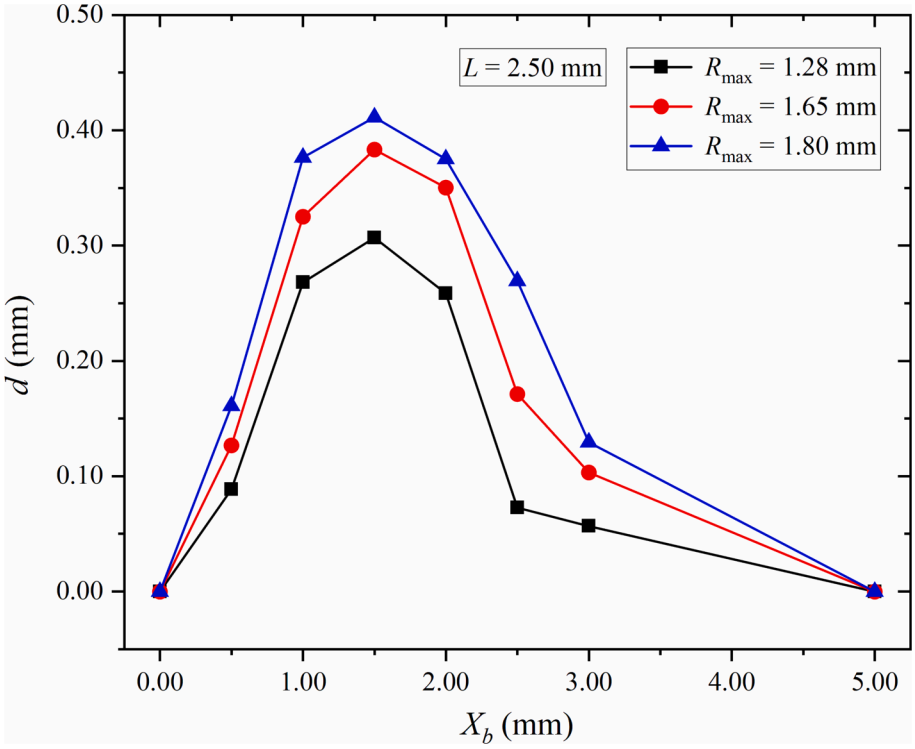

Fig. 16. The variations of the movement distance of the bubble centroid versus X_b with the different R_{max}. The blue, black and red solid lines in the figure refer to R_{max} = 1.80 mm, R_{max} = 1.28 mm and R_{max} = 1.65 mm, respectively. L = 2.50 mm.

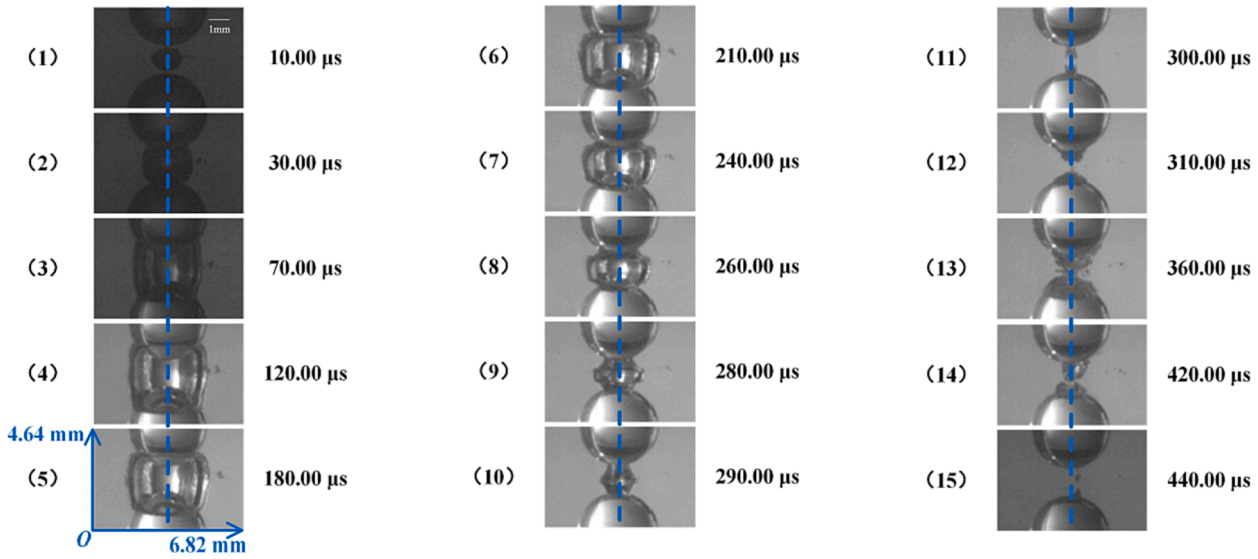

Fig. 17. Cavitation bubble dynamics on the symmetrical axis of two spherical particles of the same size. The blue dashed line refers to the initial position of bubble centroid. The subfigure at the bottom left of the figure is marked with the actual length and the width of the subfigure. $X_b = 0.00$ mm, $Y_b = 0.00$ mm, $R_{max} = 1.80$ mm, $L = 2.00$ mm and $R_p = 1.50$ mm.

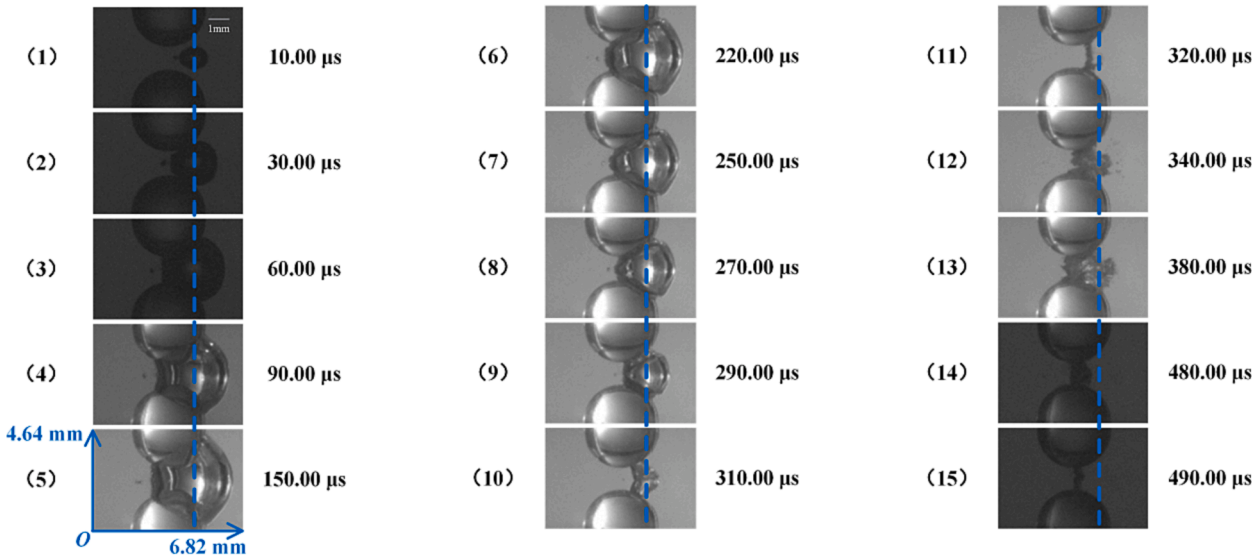

Fig. 18. Cavitation bubble dynamics on the symmetrical axis of two spherical particles of the same size. The blue dashed line refers to the initial position of bubble centroid. The subfigure at the bottom left of the figure is marked with the actual length and the width of the subfigure. $X_b = 1.00$ mm, $Y_b = 0.00$ mm, $R_{max} = 1.80$ mm, $L = 2.00$ mm and $R_p = 1.50$ mm.

between two particles are key parameters affecting morphology characteristics of the bubble collapse.

CRediT authorship contribution statement

Xiaoxiao Zheng: Conceptualization, Methodology, Investigation, Software, Writing – original draft. **Xiaoyu Wang:** Methodology, Formal analysis. **Zhiling Ding:** Resources, Validation, Software, Visualization. **Angjun Li:** Data curation, Software, Formal analysis. **Xuan Lu:** Software, Project administration. **Yuning Zhang:** Supervision, Funding acquisition, Funding acquisition.

Declaration of Competing Interest

The authors declare that they have no known competing financial interests or personal relationships that could have appeared to influence the work reported in this paper.

Acknowledgements

This work was financially supported by the National Natural Science Foundation of China (Project Nos.: 51976056 and 52076215).

References

[1] M. Dular, M. Petkovšek, On the mechanisms of cavitation erosion–coupling high speed videos to damage patterns, Exp. Therm Fluid Sci. 68 (2015) 359–370.
[2] D. Li, Y. Kang, X. Wang, X. Ding, Z. Fang, Effects of nozzle inner surface roughness on the cavitation erosion characteristics of high speed submerged jets, Exp. Therm Fluid Sci. 74 (2016) 444–452.
[3] W. Lauterborn, T. Kurz, Physics of bubble oscillations, Rep. Prog. Phys. 73 (10) (2010), 106501.

[4] Y. Zhang, Y. Zhang, Z. Qian, et al., A review of microscopic interactions between cavitation bubbles and particles in silt-laden flow, Renew. Sustain. Energy Rev. 56 (2016) 303–318.
[5] C. Duan, V.Y. Karelin, Abrasive Erosion And Corrosion Of Hydraulic Machinery, World Scientific, 2003.
[6] F. Hegedűs, K. Klapcsik, W. Lauterborn, U. Parlitz, R. Mettin, GPU accelerated study of a dual-frequency driven single bubble in a 6-dimensional parameter space: The active cavitation threshold, Ultrason. Sonochem. 67 (2020), 105067.
[7] O. Hamdaoui, E. Naffrechoux, Adsorption kinetics of 4-chlorophenol onto granular activated carbon in the presence of high frequency ultrasound, Ultrason. Sonochem. 16 (1) (2009) 15–22.
[8] O. Hamdaoui, E. Naffrechoux, An investigation of the mechanisms of ultrasonically enhanced desorption, AIChE J 53 (2) (2007) 363–373.
[9] K. Klapcsik, F. Hegedűs, Study of non-spherical bubble oscillations under acoustic irradiation in viscous liquid, Ultrason. Sonochem. 54 (2019) 256–273.
[10] S. Wu, Z. Zuo, H.A. Stone, et al., Motion of a free-settling spherical particle driven by a laser-induced bubble, Phys. Rev. Lett. 119 (8) (2017), 084501.
[11] L. Lv, Y. Zhang, Y. Zhang, Experimental investigations of the particle motions induced by a laser-generated cavitation bubble, Ultrason. Sonochem. 56 (2019) 63–76.
[12] S.R. Gonzalez-Avila, X. Huang, P.A. Quinto-Su, et al., Motion of micrometer sized spherical particles exposed to a transient radial flow: attraction, repulsion, and rotation, Phys. Rev. Lett. 107 (7) (2011), 074503.
[13] M.V. Bagal, P.R. Gogate, Wastewater treatment using hybrid treatment schemes based on cavitation and Fenton chemistry: a review, Ultrason. Sonochem. 21 (1) (2014) 1–14.
[14] M. Gągol, A. Przyjazny, G. Boczkaj, Wastewater treatment by means of advanced oxidation processes based on cavitation–a review, Chem. Eng. J. 338 (2018) 599–627.
[15] Y. Zhang, F. Chen, Y. Zhang, Y. Zhang, X. Du, Experimental investigations of interactions between a laser-induced cavitation bubble and a spherical particle, Exp. Therm Fluid Sci. 98 (2018) 645–661.
[16] X. Wang, G. Wu, X. Zheng, X. Du, Y. Zhang, Theoretical investigation and experimental support for the cavitation bubble dynamics near a spherical particle based on Weiss theorem and Kelvin impulse, Ultrason. Sonochem. 89 (2022), 106130.
[17] Y. Zhang, X. Xie, Y. Zhang, Y. Zhang, X. Du, Experimental study of influences of a particle on the collapsing dynamics of a laser-induced cavitation bubble near a solid wall, Exp. Therm Fluid Sci. 105 (2019) 289–306.
[18] J.R. Blake, P. Cerone, A note on the impulse due to a vapour bubble near a boundary, The ANZIAM Journal 23 (4) (1982) 383–393.
[19] J.R. Blake, B.B. Taib, G. Doherty, Transient cavities near boundaries. Part 1. Rigid boundary, J. Fluid Mech. 170 (1986) 479–497.
[20] J.R. Blake, B.B. Taib, G. Doherty, Transient cavities near boundaries Part 2. Free surface, J. Fluid Mech. 181 (1987) 197–212.
[21] J.R. Blake, D.C. Gibson, Cavitation bubbles near boundaries, Annu. Rev. Fluid Mech. 19 (1) (1987) 99–123.
[22] J.R. Blake, The Kelvin impulse: application to cavitation bubble dynamics, The ANZIAM Journal 30 (2) (1988) 127–146.
[23] J.R. Blake, D.M. Leppinen, Q. Wang, Cavitation and bubble dynamics: the Kelvin impulse and its applications, Interface Focus 5 (5) (2015) 20150017.
[24] J.P. Best, J.R. Blake, An estimate of the Kelvin impulse of a transient cavity, J. Fluid Mech. 261 (1994) 75–93.
[25] L. Landweber, T. Miloh, Unsteady Lagally theorem for multipoles and deformable bodies, J. Fluid Mech. 96 (1) (1980) 33–46.
[26] L.M. Milne-Thomson, Theoretical hydrodynamics, London Macmillan &, Co Ltd., 1960.
[27] Y. Zhang, Z. Sun, Review on progress of the interactions between cavitation bubble and boundary, Nucl. Sci. Eng. 42 (03) (2022) 598–615.
[28] J. P. Best, The dynamics of underwater explosions. University of Wollongong Thesis Collections. 1993.
[29] Y. Tagawa, I.R. Peters, Bubble collapse and jet formation in corner geometries, Phys. Rev. Fluids 3 (8) (2018), 081601.
[30] J. Zevnik, M. Dular, Cavitation bubble interaction with a rigid spherical particle on a microscale, Ultrason. Sonochem. 69 (2020), 105252.
[31] X. Zhang, Y. Zhang, Experimental investigation of the influences of the spherical particle on the jet formation of the cavitation bubble near the solid boundary, Mech. Eng. 43 (4) (2021) 506.
[32] G.L. Chahine, A. Kapahi, J.K. Choi, C.T. Hsiao, Modeling of surface cleaning by cavitation bubble dynamics and collapse, Ultrason. Sonochem. 29 (2016) 528–549.
[33] Y. Ma, Z. Zeng, W. Xu, L. Bai, Directional transport and random motion of particles in ALF ultrasonic cavitation structure, Ultrason. Sonochem. 72 (2021), 105439.
[34] G. Liu, H. Bie, Z. Hao, Y. Wang, W. Ren, Z. Hua, Characteristics of cavitation onset and development in a self-excited fluidic oscillator, Ultrason. Sonochem. 86 (2022), 106018.
[35] L.D. Landau, E.M. Lifshitz, Fluid Mechanics: Landau and Lifshitz: Course of Theoretical Physics, 6, Elsevier, 2013.